INTERNATIONAL JOURNAL FOR NUMERICAL METHODS IN FLUIDS, VOL. 21, 1017–1039 (1995)

AN APPLICATION OF ROE'S FLUX-DIFFERENCE SPLITTING FOR k-ε TURBULENCE MODEL

TIMO SIIKONEN

Laboratory of Aerodynamics, Helsinki University of Technology, Sähkömiehentie 4, 02150 Espoo, Finland

SUMMARY

In this paper Roe's flux-difference splitting is applied for the solution of Reynolds-averaged Navier–Stokes equations. Turbulence is modelled using a low-Reynolds number form of the k-ε tubulence model. The coupling between the turbulence kinetic energy equation and the inviscid part of the flow equations is taken into account. The equations are solved with a diagonally dominant alternating direction implicit (DDADI) factorized implicit time integration method. A multigrid algorithm is used to accelerate the convergence. To improve the stability some modifications are needed in comparison with the application of an algebraic turbulence model. The developed method is applied to three different test cases. These cases show the efficiency of the algorithm, but the results are only marginally better than those obtained with algebraic models.

KEY WORDS: turbulence models; flux-difference splitting; multigrid method; transonic turbulent flow

1. INTRODUCTION

During the past two decades k-ε turbulence modelling[1] has become a standard procedure in solving incompressible, turbulent flows in industrial applications. In aerodynamical applications with a high Reynolds number the use of the k-ε model has not been a particularly common approach. Instead, simple algebraic models like the Baldwin–Lomax model[2] are popular. Algebraic models have gained popularity because the results are often comparable with the results of more complicated models. In addition, the standard k-ε approach cannot be extended onto the wall surface; inside the boundary layer a low-Reynolds number modification is required. The turbulence transport equations contain stiff source terms. Consequently, the implementation of the model into compressible flow solvers is a difficult task. Additional numerical difficulties arise because with a high Reynolds number, turbulence is significant only inside a thin boundary layer and the turbulence quantities may vary by orders of magnitude within a very short distance.

However, the application of the algebraic models for complex geometries or wakes is not straightforward and often the resulting turbulent viscosities are not physically realistic. Special care must be taken when an algebraic model is applied for a new complex flow case. Usually a turbulence model based on differential equations is a more natural approach, although the results are not always better than those obtained with tuned algebraic modelling. Because of this, in recent years attention has been paid to the k-ε model in aerodynamic simulations also. There are many applications for turbulent flows over projectiles, see e.g. Reference 3. The k-ε model forms the basis for the algebraic Reynolds stress model. With the algebraic Reynolds stress model promising results have been obtained for flows over an airfoil.[4]

CCC 0271–2091/95/111017–23

Received August 1994
Revised February 1995

In this study, Chien's low-Reynolds number k-ε model[5] is coupled with a compressible flow solver based on Roe's method.[6] The objective of the study has been to extend the efficient solution methods of the existing Navier–Stokes solver for the turbulence transport equations, and to couple these with the flow equations. The developed scheme utilizes a finite-volume approach with a cell-centred location of the dependent variables. The solution is based on a DDADI-factorized implicit time integration method.[7] The code utilizes a multigrid V-cycle for the acceleration of convergence and is able to handle multiblock grids. The main features of the solution method are described in Reference 8.

The turbulence equations and the flow equations are coupled via the turbulent viscosity and also via the $(2\rho k/3)$ term in the momentum and energy equation.[9] The coupling through the kinetic energy term is usually neglected.[3,4] In the present study, this coupling is taken into account in applying Roe's approximative Riemann solver, and coupling is also present in the implicit stage of the solution. This coupling is fairly trivial and was taken into account for the sake of completeness, although in most cases its effect on the solution is small. Because the turbulence equations are included, modifications are required in the original scheme. The main emphasis of this paper is on these modifications. In the following, the basic features of the developed algorithm are described in detail. The method is applied for flows over a flat plate, the NACA 0012 airfoil and a delta wing.

2. NUMERICAL METHOD

2.1. Governing equations

The Reynolds-averaged Navier–Stokes equations, and the equations for the kinetic energy (k) and dissipation (ε) of turbulence can be written in the following form

$$\frac{\partial U}{\partial t}+\frac{\partial (F-F_v)}{\partial x}+\frac{\partial (G-G_v)}{\partial y}+\frac{\partial (H-H_v)}{\partial z}=Q, \tag{1}$$

where $U=(\rho, \rho u, \rho v, \rho w, E, \rho k, \rho \varepsilon)^T$. The inviscid fluxes are

$$F=\begin{pmatrix} \rho u \\ \rho u^2+p+\frac{2}{3}\rho k \\ \rho vu \\ \rho wu \\ (E+p+\frac{2}{3}\rho k)u \\ \rho uk \\ \rho u\varepsilon \end{pmatrix}, \quad G=\begin{pmatrix} \rho v \\ \rho uv \\ \rho v^2+p+\frac{2}{3}\rho k \\ \rho wv \\ (E+p+\frac{2}{3}\rho k)v \\ \rho vk \\ \rho v\varepsilon \end{pmatrix}, \quad H=\begin{pmatrix} \rho w \\ \rho uw \\ \rho vw \\ \rho w^2+p+\frac{2}{3}\rho k \\ (E+p+\frac{2}{3}\rho k)w \\ \rho wk \\ \rho w\varepsilon \end{pmatrix}. \tag{2}$$

Here ρ is the density; the velocity is $\vec{V}=u\vec{i}+w\vec{j}+w\vec{k}$; p is the pressure, and E the total internal energy defined as

$$E=\rho e+\frac{\rho \vec{V}\cdot\vec{V}}{2}+\rho k, \tag{3}$$

where e is the integral energy. The source term Q has non-zero components, which will be given later, only for turbulence equations. The viscous fluxes are

$$F_v = \begin{pmatrix} 0 \\ \tau_{xx} \\ \tau_{xy} \\ \tau_{xz} \\ u\tau_{xx} + v\tau_{xy} + w\tau_{xz} - q_x \\ \mu_k \dfrac{\partial k}{\partial x} \\ \mu_\varepsilon \dfrac{\partial \varepsilon}{\partial x} \end{pmatrix}, \quad G_v = \begin{pmatrix} 0 \\ \tau_{xy} \\ \tau_{yy} \\ \tau_{yz} \\ u\tau_{xy} + v\tau_{yy} + w\tau_{yz} - q_y \\ \mu_k \dfrac{\partial k}{\partial y} \\ \mu_\varepsilon \dfrac{\partial \varepsilon}{\partial y} \end{pmatrix},$$

$$H_v = \begin{pmatrix} 0 \\ \tau_{xz} \\ \tau_{yz} \\ \tau_{zz} \\ u\tau_{xz} + v\tau_{yz} + w\tau_{zz} - q_z \\ \mu_k \dfrac{\partial k}{\partial z} \\ \mu_\varepsilon \dfrac{\partial \varepsilon}{\partial z} \end{pmatrix}. \tag{4}$$

Boussinesq's approximation

$$-\overline{\rho u_i'' u_j''} = \mu_T \left[\frac{\partial u_j}{\partial x_i} + \frac{\partial u_i}{\partial x_j} - \tfrac{2}{3} (\nabla \cdot \vec{V}) \delta_{ij} \right] - \tfrac{2}{3} \rho k \delta_{ij}, \tag{5}$$

where μ_T is a turbulent viscosity coefficient, is applied for the Reynolds stresses. In the momentum and energy equations the kinetic energy contribution has been connected with pressure and appears in the convective fluxes, whereas the diffusive part is connected with the viscous fluxes. The heat flux is written as

$$\vec{q} = -(k + k_T) \nabla T = -\left(\mu \frac{c_p}{Pr} + \mu_T \frac{c_p}{Pr_T} \right) \nabla T, \tag{6}$$

where k is a molecular and k_T a turbulent thermal conductivity coefficient and Pr is a laminar and Pr_T a turbulent Prandtl number respectively. In this study $Pr = 0{\cdot}72$ and $Pr_T = 0{\cdot}9$ are used. The molecular viscosity μ is calculated from Sutherland's formula. The diffusion of turbulence variables is modelled as

$$\mu_k \nabla k = \left(\mu + \frac{\mu_T}{\sigma_k} \right) \nabla k, \tag{7}$$

$$\mu_\varepsilon \nabla \varepsilon = \left(\mu + \frac{\mu_T}{\sigma_\varepsilon} \right) \nabla \varepsilon, \tag{8}$$

where σ_k and σ_ε are empirical coefficients. The pressure is calculated from the perfect gas law

$$p = (\gamma - 1) \rho e, \tag{9}$$

where γ is the ratio of specific heats c_p/c_v.

The equations are scaled with free-stream speed of sound c_∞, density ρ_∞, temperature T_∞, viscosity μ_∞ and reference length L_∞. In particular, the non-dimensionalized kinetic energy and dissipation of turbulence are expressed as $k^* = k/c_\infty^2$ and $\varepsilon^* = \varepsilon/(c_\infty^3/L_\infty)$. The present scaling retains the form of the inviscid fluxes, whereas the stress terms have to be multiplied by Ma_∞/Re_∞ and the non-dimensionalized heat flux term becomes

$$\vec{q} = \frac{Ma_\infty}{Re_\infty(\gamma-1)}\left(\mu\frac{c_p}{Pr} + \mu_T\frac{c_p}{Pr_T}\right)\nabla T \tag{10}$$

Here, and in the following, scaled variables are used and the superscripts have been dropped for simplicity.

2.2. *Turbulence modelling*

In this study the solution is extended to the wall instead of using a wall-function approach. Near the wall the low-Reynolds number model proposed by Chien[5] is adopted. The source term for Chien's model is given as

$$Q = \begin{pmatrix} P - \rho\varepsilon - 2\dfrac{Ma_\infty}{Re_\infty}\,\mu\,\dfrac{k}{y_n^2} \\ \\ c_1\,\dfrac{\varepsilon}{k}\,P - c_2\,\dfrac{\rho\varepsilon^2}{k} - 2\,\dfrac{Ma_\infty}{Re_\infty}\,\mu\,\dfrac{\varepsilon}{y_n^2}\,e^{-y^+/2} \end{pmatrix}, \tag{11}$$

where y_n is the normal distance from the wall, and y^+ is calculated from

$$y^+ = \left(\frac{Re_\infty}{Ma_\infty}\right)^{1/2} y_n\left[\frac{\rho|\nabla\times\vec{V}|}{\mu}\right]_{\text{wall}}^{1/2}. \tag{12}$$

The wall quantities are taken from the first cell above the wall surface.

The product of turbulent kinetic energy is modelled using (5) as

$$P = -\rho u_i'' u_j''\frac{\partial u_i}{\partial x_j} = \left[\mu_T\left(\frac{\partial u_i}{\partial x_j} + \frac{\partial u_j}{\partial x_i} - \tfrac{2}{3}\delta_{ij}\frac{\partial u_k}{\partial x_k}\right) - \tfrac{2}{3}\delta_{ij}\rho k\right]\frac{\partial u_i}{\partial x_j}, \tag{13}$$

which can be rewritten in the following non-dimensionalized form

$$P = \frac{Ma_\infty}{Re_\infty}\mu_T\left\{2\left(\left(\frac{\partial u}{\partial x}\right)^2 + \left(\frac{\partial v}{\partial y}\right)^2 + \left(\frac{\partial w}{\partial z}\right)^2\right] + \left(\frac{\partial u}{\partial y} + \frac{\partial v}{\partial x}\right)^2$$

$$+\left(\frac{\partial u}{\partial z} + \frac{\partial w}{\partial x}\right)^2 + \left(\frac{\partial v}{\partial z} + \frac{\partial w}{\partial y}\right)^2 - \tfrac{2}{3}\left(\nabla\cdot\vec{V}\right)^2\right\} - \tfrac{2}{3}\rho k\nabla\cdot\vec{V}, \tag{14}$$

where $(u, v, w) = (u_1, u_2, u_3)$, $(x, y, z) = (x_1, x_2, x_3)$ and $\vec{V} = u\vec{i} + v\vec{j} + w\vec{k}$. Above, the production term is non-dimensionalized as $P^* = P/(\rho_\infty c_\infty^3/L_\infty)$.

In the k-ε model the turbulent viscosity is calculated from

$$\mu_T = c_\mu\frac{\rho k^2}{\varepsilon}\frac{Re_\infty}{Ma_\infty}. \tag{15}$$

The formulae given above contain empirical coefficients. These are given by

$$c_1 = 1{\cdot}44, \quad c_2 = 1{\cdot}92(1 - 0{\cdot}22e^{-Re_T^2/36}), \quad \sigma_k = 1{\cdot}0, \quad \sigma_\varepsilon = 1{\cdot}3, \quad c_\mu = 0{\cdot}09(1 - e^{-0{\cdot}0115y^+}),$$

where the turbulence Reynolds number is defined as

$$Re_T = \frac{\rho k^2}{\mu\varepsilon}\frac{Re_\infty}{Ma_\infty}. \tag{16}$$

Chien proposed slightly different forms for c_1 and c_2. Since the computations performed for the flat plate boundary layer appeared to be insensitive to the modifications, the formulae above were based on the most commonly used coefficients $c_1 = 1{\cdot}44$ and $c_2 = 1{\cdot}92$.

2.3. *Spatial discretization*

In the present solution, a finite-volume technique is applied. The flow equations have an integral form

$$\frac{\mathrm{d}}{\mathrm{d}t}\int_V U\mathrm{d}V + \int_S \vec{F}(U)\cdot\mathrm{d}\vec{S} = \int_V Q\mathrm{d}V \tag{17}$$

for an arbitrary fixed region V with a boundary S. Performing the integrations for a computational cell i yields

$$V_i\frac{\mathrm{d}U_i}{\mathrm{d}t} = -\sum_{\text{faces}} S\hat{F} + V_iQ_i, \tag{18}$$

where the sum is taken over the faces of the computational cell. The flux on the cell face is

$$\hat{F} = n_xF + n_yG + n_zH. \tag{19}$$

Here F, G and H are the fluxes defined by (2)–(4), and n_x, n_y, n_z are the components of the unit normal vector in the x-, y- and z-directions respectively. In the evaluation of the inviscid fluxes Roe's method[6] is employed. The flux is calculated as

$$\hat{F} = T^{-1}F(TU), \tag{20}$$

where T is a rotation matrix which transforms the dependent variables to a local co-ordinate system normal to the cell surface. In this way only the Cartesian form F of the flux is needed. This is calculated from

$$F(U^{\mathrm{l}}, U^{\mathrm{r}}) = \tfrac{1}{2}[F(U^{\mathrm{l}}) + F(U^{\mathrm{r}})] - \tfrac{1}{2}\sum_{k=1}^{K} r^{(k)}|\lambda^{(k)}|\alpha^{(k)}, \tag{21}$$

where U^{l} and U^{r} are the solution vectors evaluated on the left and right sides of the cell surface, $r^{(k)}$ is a right eigenvector of the Jacobian matrix $A = \partial F/\partial U = R\Lambda R^{-1}$, the corresponding eigenvalue is $\lambda^{(k)}$, and $\alpha^{(k)}$ is the corresponding characteristic variable obtained from $R^{-1}\Delta U$, where $\Delta U = U^{\mathrm{r}} - U^{\mathrm{l}}$. A MUSCL-type approach has been adopted for the evaluation of U^{l} and U^{r}. In the evaluation of U^{l} and U^{r}, primary flow variables (ρ, u, v, w, p), and conservative turbulent variables (ρk, $\rho\varepsilon$) are utilized.

In this case the eigenvalues, i.e. the characteristic speeds, are

$$\lambda_{1,2,3,4,5,6,7} = u, u + c, u, u, u - c, u, u, \tag{22}$$

where c is the speed of sound. The k-ε model introduces a coupling between the flow equations and turbulence equations via the $(2\rho k/3)$ term in the momentum and energy equations.[9] This coupling changes the formulae for $r^{(k)}$, $\lambda^{(k)}$, and $\alpha^{(k)}$. In the present study the $(2\rho k/3)$ term is taken into account,

although its effect may be small in most flow cases. If the $(2\rho k/3)$ term were neglected from the eigenvector analysis, k would be centrally differenced in the inviscid part of the momentum and energy equations. In that case there would be a possibility for a 'sawtooth'-like solutions, especially when $(2\rho k/3)$ is significant in comparison with pressure. It should also be noted that the damping term of (21) is evidently in many ways unnecessarily complicated, at least with low Mach-numbers. Fortunately, this complexity is not too expensive in computational terms, thus there is no actual need for simplifications.

By taking into account the contribution of turbulence, the speed of sound can be written for an arbitrary equation of state as

$$c^2 = \frac{\partial p}{\partial \rho} + \frac{p}{\rho^2}\frac{\partial p}{\partial e} + \tfrac{2}{3}k\left(\frac{1}{\rho}\frac{\partial p}{\partial e} + 1\right). \tag{23}$$

With a perfect gas assumption this reduces to

$$c^2 = \frac{\gamma}{\rho}[p + \tfrac{2}{3}\rho k]. \tag{24}$$

The characteristic variables are

$$\begin{aligned}
\alpha^{(1)} &= \left(1 - \frac{2}{3}\frac{k}{c^2}\right)\delta\rho - \frac{1}{c^2}\delta p - \frac{2}{3}\frac{\rho}{c^2}\delta k,\\
\alpha^{(2)} &= \frac{1}{2c^2}(\tfrac{2}{3}k\delta\rho + \rho c\delta u + \delta p + \tfrac{2}{3}\rho\delta k),\\
\alpha^{(3)} &= \rho\delta v,\\
\alpha^{(4)} &= \rho\delta w,\\
\alpha^{(5)} &= \frac{1}{2c^2}(\tfrac{2}{3}k\delta\rho - \rho c\delta u + \delta p + \tfrac{2}{3}\rho\delta k),\\
\alpha^{(6)} &= \rho\delta k,\\
\alpha^{(7)} &= \rho\delta\varepsilon,
\end{aligned} \tag{25}$$

and the right eigenvector matrix is

$$R = \begin{pmatrix}
1 & 1 & 0 & 0 & 1 & 0 & 0\\
u & u+c & 0 & 0 & u-c & 0 & 0\\
v & v & 1 & 0 & v & 0 & 0\\
w & w & 0 & 1 & w & 0 & 0\\
h - \dfrac{\rho c^2}{\partial p/\partial e} & h+uc & v & w & h-uc & 1 - \dfrac{2}{3}\dfrac{\rho}{\partial p/\partial e} & 0\\
k & k & 0 & 0 & k & 1 & 0\\
\varepsilon & \varepsilon & 0 & 0 & \varepsilon & 0 & 1
\end{pmatrix}. \tag{26}$$

For a perfect gas $\partial p/\partial e = (\gamma - 1)\rho$. The total enthalpy is defined as

$$h = (E + p)/\rho + \tfrac{2}{3}k. \tag{27}$$

2.4. *Calculation of the viscous fluxes and the source term*

The viscous fluxes as well as the drivatives in (14) are evaluated using a thin-layer approximation. For example, in the calculation of P, the velocity derivatives are approximated in the i-direction as

$$\left(\frac{\partial u}{\partial x}\right)_i = \frac{(Sn_x u)_{i+1/2} - (Sn_x u)_{i-1/2}}{V_i} \approx \frac{(n_x u)_{i+1/2} - (n_x u)_{i-1/2}}{d_i}, \tag{28}$$

where d_i is the cell thickness in the i-direction. Velocities at the cell surfaces are obtained as averages from the nodal values. Using the thin-layer approximation a lot of complexity in programming is avoided and computation time is saved. With a high Reynolds number the results obtained by the thin-layer approximation are practically the same as with a more accurate computation of the derivatives. In the computer code, the thin-layer model can be activated in desired co-ordinate directions. For the derivatives in the viscous fluxes on the surface $i+1/2$, (28) is applied for a shifted control volume $V_{i+1/2}$.

The source term and the possible wall correction in c_μ are calculated similarly in the i-, j- and k-directions. As a result, the source term may contain several wall terms, and the wall correction of turbulent viscosity is different in different coordinate directions if walls are present.

2.5. *Boundary conditions*

At the free-stream boundary the values of the dependent variables are kept as constants. In the calculation of the inviscid fluxes at the solid boundary, flux-difference splitting is not used. Since the convective speed is equal to zero on the solid surfaces, the only contribution to the inviscid surface fluxes arises from the pressure terms in the momentum equations. A second-order extrapolation from the flow field is applied for the evaluation of the wall pressure.

The viscous fluxes on the solid surfaces are obtained by setting $u=v=w=0$ on the wall. The central expression of the viscous terms is replaced by a second-order one-sided formula. The wall temperature is either set to a free-stream stagnation temperature or the wall is assumed to be adiabatic. The viscous fluxes of k and ε are also set to zero at the wall. In this way, there is no need to specify the surface values of the turbulence quantities.

2.6. *Solution algorithm*

The discretized equations are integrated in time by applying the DDADI-factorization.[7] This is based on the approximate factorization and on the splitting of the Jacobians of the flux terms. The resulting implicit stage consists of a backward and forward sweep in every coordinate direction. The sweeps are based on a first-order upwind differencing. In addition, the linearization of the source term is factored out of the spatial sweeps. The boundary conditions are treated explicitly, and a spatially varying time step is utilized.

The implicit stage can be written after factorization as follows

$$\left[I + \frac{\Delta t}{V_i}\left(\partial_i^- S_{i+1/2} A_i^+ - \partial_i^+ S_{i-1/2} A_i^-\right)\right]\left[I + \frac{\Delta t}{V_j}\left(\partial_j^- S_{j+1/2} B_j^+ - \partial_j^+ S_{j-1/2} B_j^-\right)\right]$$

$$\times\left[I + \frac{\Delta t}{V_k}(\partial_k^- S_{k+1/2} C_k^+ - \partial_k^+ S_{k-1/2} C_k^-)\right][I - \Delta t D_i]\Delta U_i = \frac{\Delta t}{V_i}\mathscr{R}_i \tag{29}$$

where $\partial_{i,j,k}^-$ and $\partial_{i,j,k}^+$ are first-order backward and forward spatial difference operators in the i, j and k directions, A, B and C are the corresponding Jacobian matrices, $D=\partial Q/\partial U$, and $\mathscr{R}_i$ is the right-hand

side of (18). The Jacobians are calculated as

$$A^{\pm} = R(|\Lambda^{\pm}| + kI)R^{-1}, \tag{30}$$

where $\Lambda^{\pm}$ are diagonal matrices containing the positive and negative eigenvalues and k is a factor to ensure the stability of the viscous term. The idea of the diagonally dominant factorization is to put as much weight on the diagonal as possible. In the i-direction the tridiagonal equation set resulting from (29) is replaced by two bidiagonal sweeps and a matrix multiplication

$$\begin{aligned}
&(V_i + \Delta t S_{i-1/2}|A|_i)\Delta U_i^{**} - \Delta t S_{i+1/2} A_{i+1}^{-} \Delta U_{i+1}^{**} = \Delta t \mathscr{R}_i, \\
&(V_i + \Delta t S_{i-1/2} A_i^{+} - \Delta t S_{i+1/2} A_i^{-})^{-1} V_i \Delta U_i^{*} = \Delta U_i^{**}, \\
&(V_i + \Delta t S_{i+1/2}|A|_i)\Delta U_i - \Delta t S_{i-1,2} A_{i-1}^{+} \Delta U_{i-1} = V_i \Delta U_i^{*},
\end{aligned} \tag{31}$$

Similar sweeps are performed in the j- and k-directions. Some computation time is saved by using the primitive variables instead of the conservative variables during the spatial sweeps.

The matrix inversion resulting from the source-term linearization is performed before the spatial sweeps. Several forms have been suggested for the Jacobian matrix D. To improve stability, only negative source terms can be linearized. Although the form of the source term indicates that equations may become stiff near the walls, the terms related to the walls are not linearized here. Thus, the only contribution arises from the dissipation terms of (11). As in Reference 9 the dissipation is written in the k-equation as

$$-\rho\varepsilon = -\frac{Re_\infty}{Ma_\infty}\frac{c_\mu}{\mu_T}(\rho k)^2. \tag{32}$$

Since the production term is positive, its linearization is not possible. However, there is a strong coupling between the flow field, turbulent viscosity and the production term P. The stiffness caused by the production term can be reduced by using the following pseudolinearization

$$\frac{\partial P}{\partial U} = -\frac{P}{|\Delta U_{\max}|}. \tag{33}$$

The idea of this is to limit the maximum change of U caused by P to $|\Delta U_{\max}|$. The resulting Jacobian of the source term is

$$\frac{\partial Q}{\partial U} = \begin{pmatrix} -\dfrac{|P|}{|\Delta(\rho k)_{\max}|} - 2\dfrac{\varepsilon}{k} & 0 \\ 0 & \dfrac{-c_1(\varepsilon/k)|P|}{|\Delta(\rho\varepsilon)_{\max}|} - 2c_2\dfrac{\varepsilon}{k} \end{pmatrix} \tag{34}$$

The maximum changes $|\Delta U_{\max}|$ are evaluated using the current values of ρk and $\rho\varepsilon$ as

$$|\Delta(\rho k)_{\max}| = \rho k / C_k, \quad |\Delta(\rho\varepsilon)_{\max}| = \rho\varepsilon / C_\varepsilon. \tag{35}$$

Since the turbulent viscosity is twice as sensitive to changes of k as to changes of ε, in the present study C_ε was set to 5, and $C_k = 2C_\varepsilon$.

With an algebraic turbulence model the scheme is stable with Courant numbers of $O(10)$. When the flow is fully turbulent, the application of the k-ε model does not essentially reduce the stability limit. However, there is a fundamental difficulty in the simulation of external flows, where large regions of laminar flow are connected with turbulent regions near the flying vehicle and the wake. The values of the turbulence quantities may vary by orders of magnitude within a short distance. Occasionally, a tiny change Δk may be much larger than the current value of k, and it is possible that a physically

unrealistically large value of μ_T would result if ε did not increase correspondingly. Since this cannot be guaranteed, some further limitations either in μ_T or in turbulence quantities is necessary. After the implicit sweeps $\Delta\rho k$ is limited to 1/6 and $\Delta\rho\varepsilon$ to 1/3 of their current values. This limitation does not significantly slow down the convergence rate. It should be noted that the robustness could also be increased by using larger values for k and ε in the free-stream. To guarantee physically reasonable values during the iteration, the maximum size of μ_T was also limited. In the present test cases the specified upper limit of μ_T was so high that the steady state results are not affected by the limitation.

For the acceleration of convergence, a multigrid cycling is employed. The method of Jameson[10] with a simple V-cycle has been adopted. The spatial discretization applied on the coarse grid levels is of the first order, which improves the stability and allows the use of a larger *CFL*-number on those grid levels. The basic implementation of the multigrid cycling is described in Reference 8 and is not changed because of the implementation of the k-ε model. However, some modifications are needed for stability reasons. The modifications concern the interpolation of k and ε corrections from a coarse grid level to a finer level, and the evaluation of the turbulent viscosity. Firstly, the size of the corrections was limited similarly to those in the basic time integration scheme, i.e. the interpolated $\Delta\rho k$ was limited to 1/6 and $\Delta\rho\varepsilon$ to 1/3 of their current values. In the airfoil calculations it was observed that the explicit treatment of the wake cut always caused troubles with the multigrid. Because of this, on the finer grid levels the corrections of the turbulence quantities are not interpolated to the first row of cells next to the grid boundaries. This treatment improves the stability, but has only a minor effect on the speed of convergence.

In transonic test calculations, the solution always finally blew up when the multigrid method was applied. This situation can be improved if on the coarse grid levels the turbulent viscosity is not calculated. Since μ_T is a non-linear function of the turbulence quantities and the shape of the boundary layer, the resulting turbulent vicosities on the coarser grid level may differ considerably from those evaluated on the fine grid level. To circumvent this, the turbulent viscosities were only calculated on the finest grid level and those values were transferred to the coarser grids. This procedure is of essential importance for the robustness of the multigrid cycle, and has no effect on the final result or the convergence.

3. COMPUTATIONAL RESULTS

3.1. Flow over a flat plate

The near-wall behaviour of the turbulence model was checked by calculating a flat plate boundary layer. The results were compared with Klebanoff's experiments.[11] The measured data is at $Re_x = 4{\cdot}2 \times 10^6$, where the corresponding boundary layer thickness is 0·0762 m. In the experiment the true distance from the leading edge of the plate was shorter, but a thickening of the boundary layer was achieved by covering the first 2 feet of the plate with sand roughness consisting of No. 16 floor-sanding paper. In this way the distance from the virtual origin was 4·328 m. In the experiment the free-stream speed was 50 feet per second. The calculations were performed at $Ma_\infty = 0{\cdot}2$ to guarantee convergence.

The computational domain was extended to cover the flat plate from the virtual origin to $x = 4{\cdot}453$. The grid size was 48×48. The height of the first row of cells was 7×10^{-5} and the grid was heavily clustered near the wall. In the axial direction the grid was clustered near the origin. From $x = 0{\cdot}453$ to $x = 4{\cdot}453$ a constant grid spacing of 0·125 was used. As a boundary condition, constant distributions were given for the flow and for the turbulence quantities. The turbulence intensity, defined as $k/(3/2\rho_\infty u_\infty^2)$, was assumed to be 0·01 and the dissipation of the turbulence was calculated by assuming $\mu_T = 0{\cdot}1$ at the free-stream. The free-stream conditions were also used as initial conditions. It

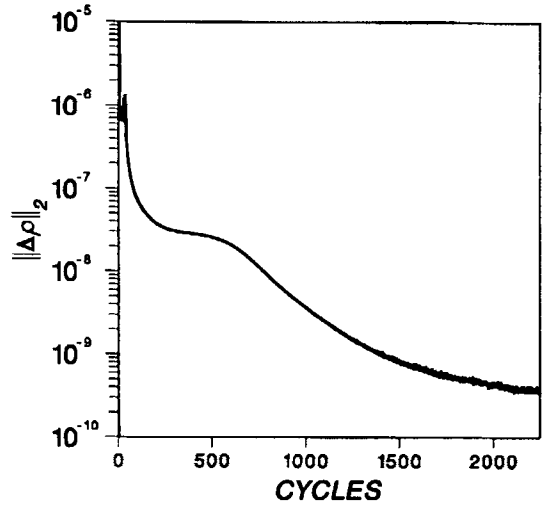

Figure 1. L_2-norm of the density residual

is difficult to specify the inlet boundary conditions according to the experiment. The wind tunnel turbulence level was lower than the value used in the simulation, but in the experiment the flow conditions were distorted because of the surface roughness at the leading edge. In spite of the evident uncertainty, no attempt was made to tune the inlet boundary conditions according to the computed results.

In this case the Courant number was 10 and three multigrid levels were applied. The convergence of the L_2-norm of the density residual is shown in Figure 1. In spite of the multigrid acceleration, the convergence is slower than with an algebraic turbulence model. With an algebraic model, turbulent viscosity is based on the local conditions; in the present case k and ε are convected throughout the domain, which is a slow process. This is evidently caused by the small time steps required by stability inside the boundary layer. Nevertheless, the convergence is significantly improved because of the multigrid. A single grid calculation required more than 10 000 iteration cycles to converge.

The distribution of the friction coefficient is shown in Figure 2. It is seen that with the specified boundary conditions there is a transition at about $x = 0{\cdot}1$. At $Re_x = 4{\cdot}2 \times 10^6$ the calculated friction coefficient is $2{\cdot}945 \times 10^{-2}$, whereas the experimental value is $2{\cdot}81 \times 10^{-2}$. The agreement between the calculation and the experiment is fairly good in spite of the fact that the boundary conditions are not accurately specified. The calculated friction coefficient is also compared with a theoretical formula.[12]

$$c_f = 0{\cdot}0468\left(\frac{\mu}{\rho U_1 \delta}\right)^{1/4}, \tag{36}$$

where U_1 is the free-stream velocity and the boundary layer thickness δ is calculated from

$$\delta = 0{\cdot}383\frac{x}{(Re_x)^{1/5}}. \tag{37}$$

The kinetic energy of turbulence at stations $Re_x = 3{\cdot}05 \times 10^6$ and $Re_x = 4{\cdot}2 \times 10^6$ is shown in Figure 3. The prediction is on a somewhat lower level than the experimental data, which may be caused by the inaccuracy in boundary conditions. The velocity profiles are compared in Figures 4 and 5. It is seen that the calculated profile obeys the logarithmic law, but the comparison with the measured

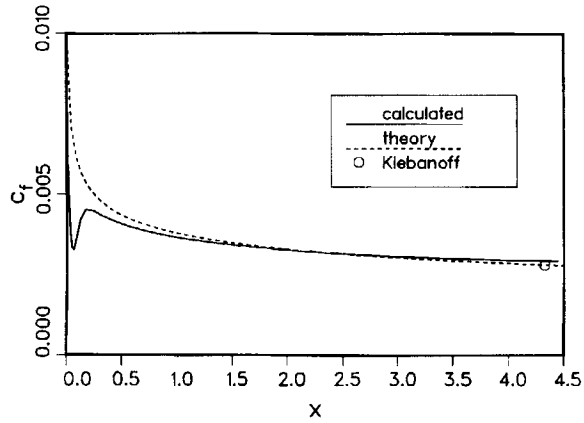

Figure 2. Comparison of the skin friction coefficients

velocity profile is not completely satisfactory. The calculated turbulence quantities as a function of y^+ are shown in Figures 6–8. The parameters of the turbulence model have some effect on the calculated results. Some modifications improved the kinetic energy profile, but the velocity profile became worse. The key parameter for the good agreement with the logarithmic law is c_μ, especially the exponent $-0{\cdot}0115y^+$. If the amplifier of y^+ in the exponent is modified slightly, say by 10%, the calculated velocity profile is no longer in accordance with the logarithmic law.

3.2. Transonic flow over the NACA 0012 airfoil

As the next case, a flow over the NACA 0012 airfoil was calculated at $Ma = 0{\cdot}799$, $Re = 9 \times 10^6$ and $\alpha = 2{\cdot}66°$. A C-type grid with 192 × 64 cells was used in the simulation. The outer boundary of the grid is 20 chord lengths from the airfoil, and the cell thicknesses on the surface varied from 5×10^{-6} at the leading edge to 2×10^{-5} at the trailing edge.

As in the flat plate calculation, the transition was not modelled. Transition could be modelled in the following way: evidently, a laminar flow is a trivial solution of the present flow model. If the initial conditions are 'sufficiently turbulent', there is possibly another solution (or even several solutions),

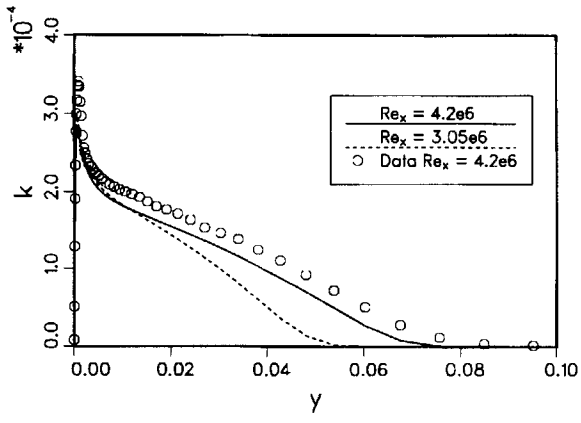

Figure 3. Kinetic energy as a function of the normal distance

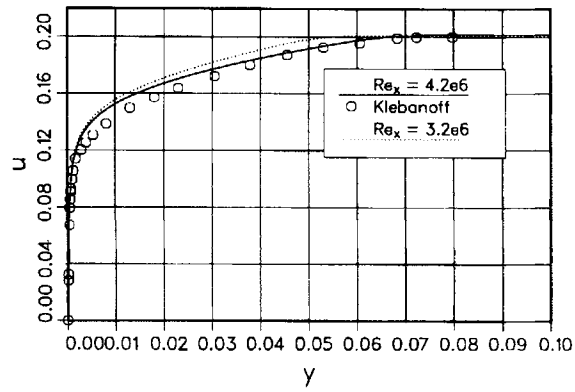

Figure 4. Calculated and experimental velocity profiles

which correspond to turbulent flow. With a suitable initial value distribution, transition can be taken into account. The reason for this possibility lies in the parabolic nature of the k- and ε-equations: turbulence cannot spread in an upstream direction. A more physical way would be the use of suitable free-stream values, as was the case with the flat plate boundary layer, and to let the turbulence model take care of the transition. However, it is questionable whether the k-ε model can be applied for the accurate prediction of transition in this way.

In this case the free-stream values of the turbulence quantities were set to $k = 4 \times 10^{-8}$ and $\varepsilon = 1 \times 10^{-8}$. The effect of the free-stream values on the solution was not studied. The initial conditions were $k = 0{\cdot}01$ and $\mu_T = 10$. Since constant initial conditions were specified all over the computational domain, a fully turbulent solution was obtained.

As far as the convergence and stability of the solution are concerned, this appears to be a tough case. The simulation was performed with three grid levels at $CFL = 2$. The difficulties were concentrated on the interaction of the shock and boundary layer and on the explicit treatment of the wake cut. The devices described in Section 2 improved the situation and a satisfactory convergence was obtained. The

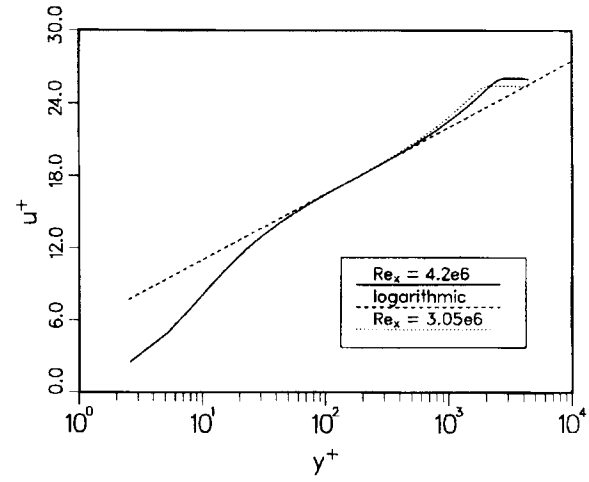

Figure 5. Comparison of calculated velocity profiles with a logarithmic law

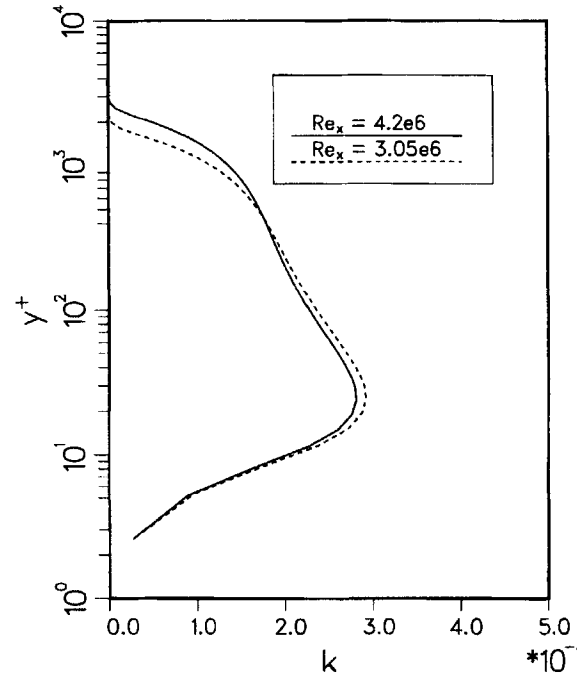

Figure 6. Kinetic energy of turbulence as function of y^+

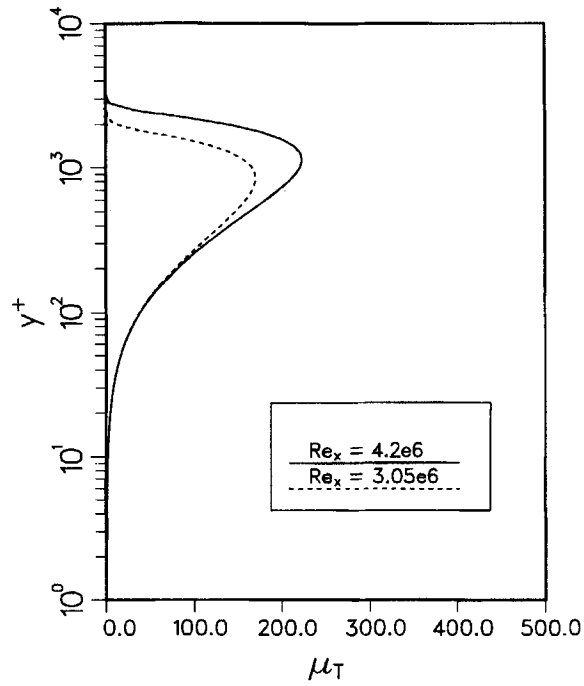

Figure 7. Dissipation of turbulence as a function of y^+

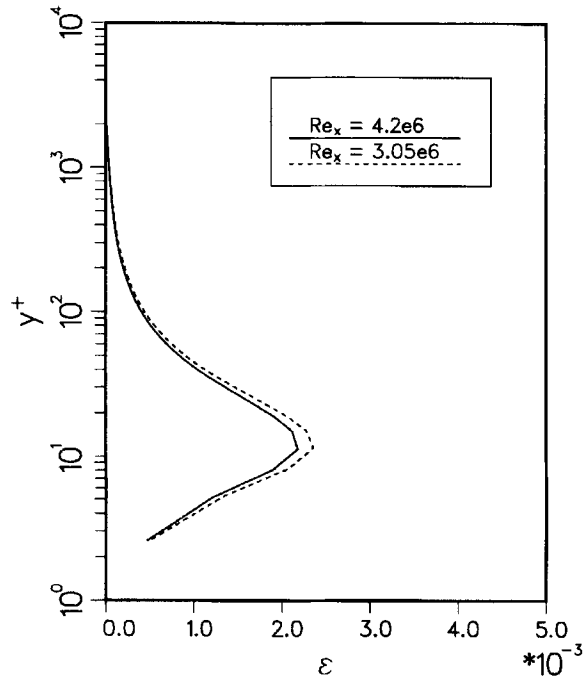

Figure 8. Turbulent viscosity distribution as a function of y^+

convergence histories of the lift and drag coefficients are shown in Figures 9 and 10. It can be seen that these coefficients are practically converged in 1 500 iteration cycles.

The Mach-number distribution is shown in Figure 11. This case has also been calculated using an algebraic Baldwin–Lomax model.[13] In the present calculations the Baldwin–Lomax model always produced a time-dependent result. Because of this the k-ε simulation was compared with the steady

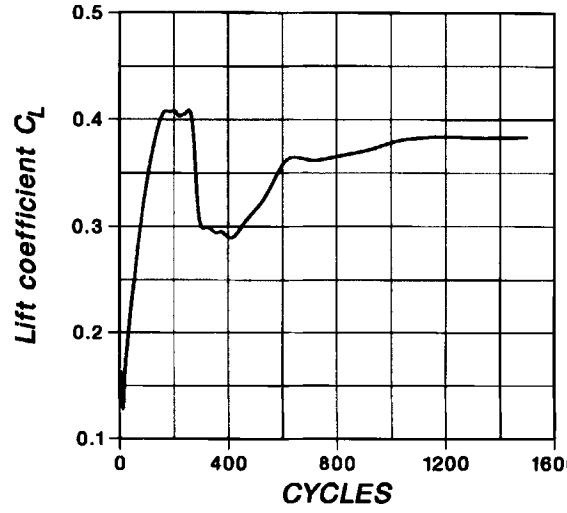

Figure 9. Convergence of the lift coefficient

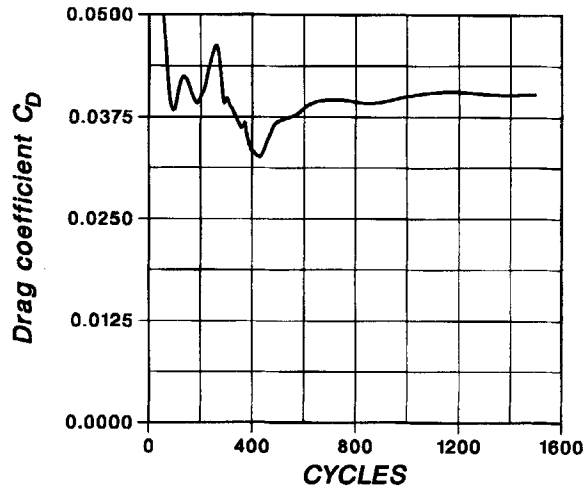

Figure 10. Convergence of the drag coefficient

results obtained by a Cebeci–Smith model.[14] The comparison of the pressure coefficient in Figure 12 shows some improvement when the k-ε model is applied. From the friction coefficient distributions in Figure 13 it can be seen that the two solutions are qualitatively different. Both models predict a shock-induced separation, but with the k-ε model there is a reattachment, whereas with the Cebeci–Smith model the flow remains separated.

The turbulence quantities as a function of y^+ are shown at three axial locations in Figures 14–17. Location $i = 100$ is close to the leading edge, $i = 125$ is just before the shock, $i = 150$ is near the trailing edge and $i = 175$ is in the wake region. It is apparent that the kinetic energy of turbulence is

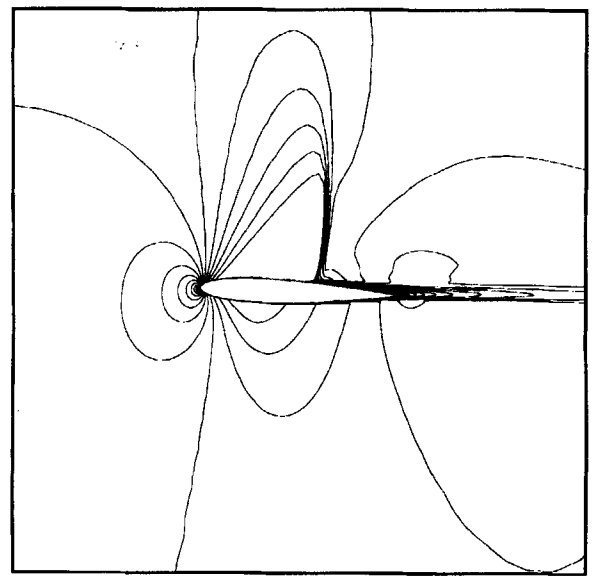

Figure 11. Mach number distribution at $Ma = 0{\cdot}799$, $Re = 9 \times 10^6$

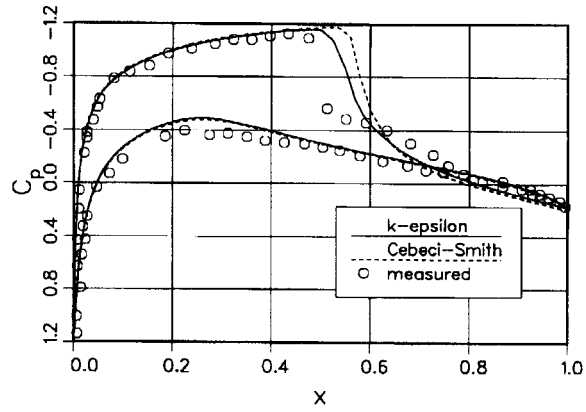

Figure 12. Pressure coefficient distribution at $Ma = 0{\cdot}799$, $Re = 9 \times 10^6$

increased after the shock location whereas the dissipation is reduced. As a result high turbulent viscosities are predicted (Figure 17).

3.3. Transonic flow over a delta wing

To test the performance of the turbulence model in a 3D-case, the flow past a cropped delta wing was calculated at $Ma_\infty = 0{\cdot}85$, $Re_\infty = 4{\cdot}5 \times 10^6$ and $\alpha = 10{\cdot}76°$. The wing selected for these calculations is the round leading edge cropped delta wing used in the International Vortex Flow Experiment on Euler Code Validation.[15] Previously, the flow pattern past this wing has been studied in References 16 and 17.

The grid used in the calculations was a single-block O–O grid with 128 × 48 × 64 cells in the chordwise, near-normal and spanwise directions respectively. The outer boundary of the grid is a sphere centred at the middle of the root chord with a radius of $10c_r$. The reference point for the pitching moment calculation is $x = 0{\cdot}57c_r$, and the reference length for the moment calculation is the root chord c_r.

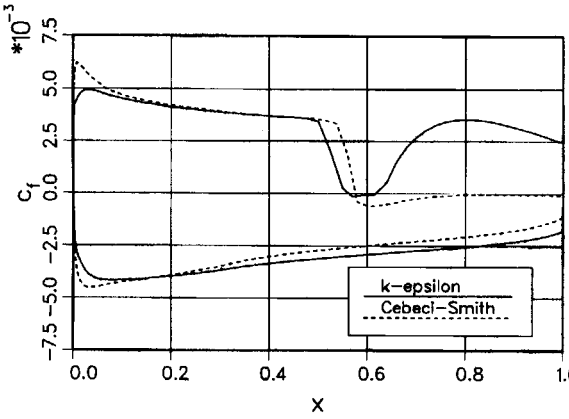

Figure 13. Friction coefficient distribution at $Ma = 0{\cdot}799$, $Re = 9 \times 10^6$

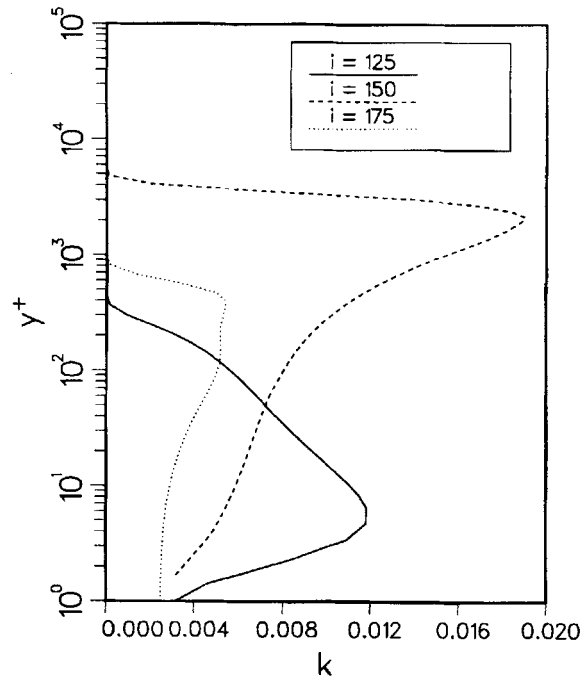

Figure 14. Kinetic energy of turbulence at three axial stations at $Ma = 0{\cdot}799$, $Re = 9 \times 10^6$

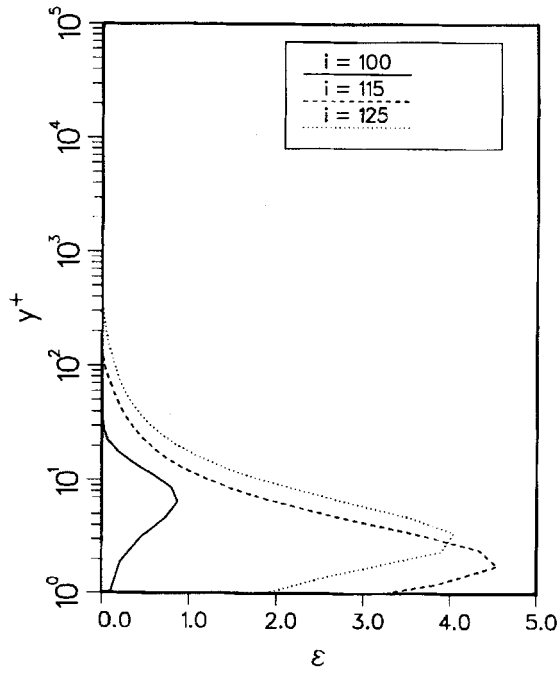

Figure 15. Dissipation of turbulence at three axial stations at $Ma = 0{\cdot}799$, $Re = 9 \times 10^6$

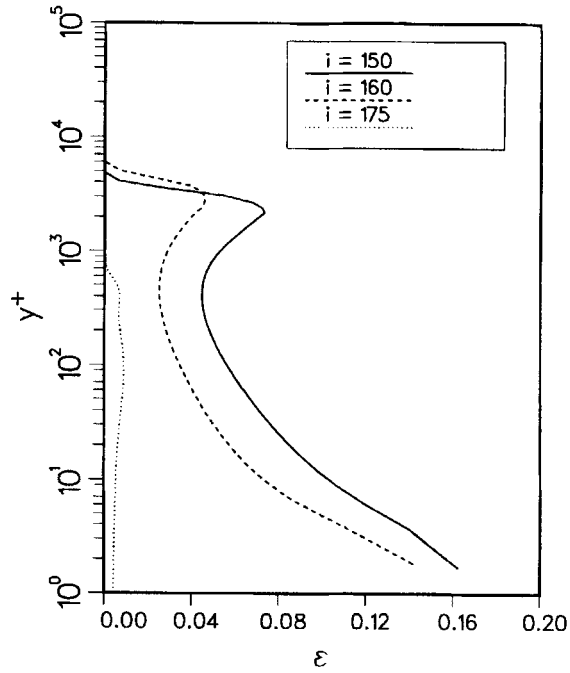

Figure 16. Dissipation of turbulence at three axial stations at $Ma = 0{\cdot}799$, $Re = 9 \times 10^6$

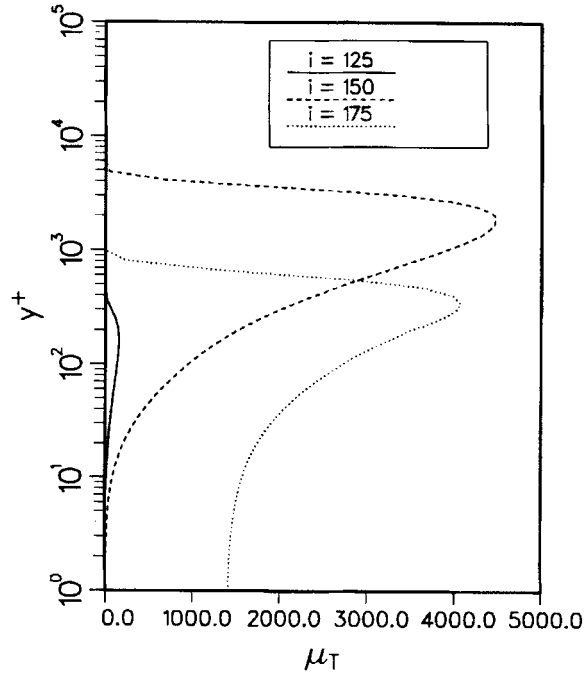

Figure 17. Turbulent viscosity at three axial stations at $Ma = 0{\cdot}799$, $Re = 9 \times 10^6$

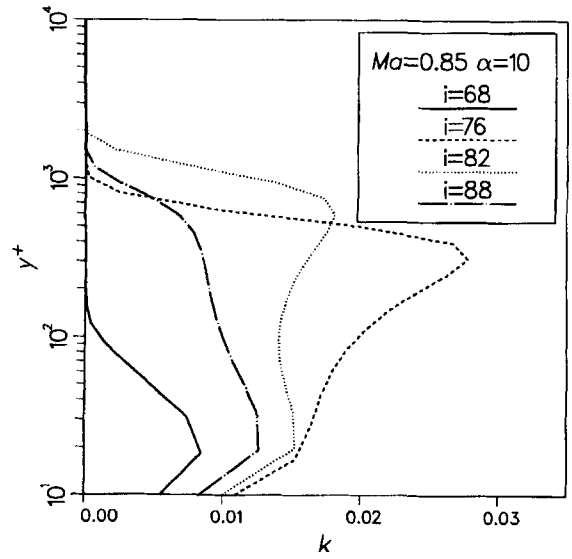

Figure 18. Profiles of kinetic energy of turbulence at $2y/b = 0{\cdot}27$

As in the previous cases, the effect of the free-stream values on the solution was not studied. The free-stream values of the turbulence quantities were set to $k = 4 \times 10^{-8}$ and $\varepsilon = 1 \times 10^{-8}$. The initial conditions were $k = 0{\cdot}38 \times 10^{-4}$ and $\mu_T = 1$. The initial conditions correspond to a turbulence intensity of 0·005.

The calculated turbulence quantities in a spanwise cross-section $2y/b = 0{\cdot}27$, where b is the wing span, are shown in Figures 18–20. The first station from which data is taken, $i = 68$, is right behind the leading edge on the upper surface, and $i = 88$ is at $(x/c)_{\text{local}} \approx 0{\cdot}37$. The turbulence kinetic energy is shown in Figure 19. A distinct peak after $i = 76$ is seen to develop owing to the turbulence generation caused by the primary vortex. The turbulent viscosity distributions in Figure 20 form a set of almost

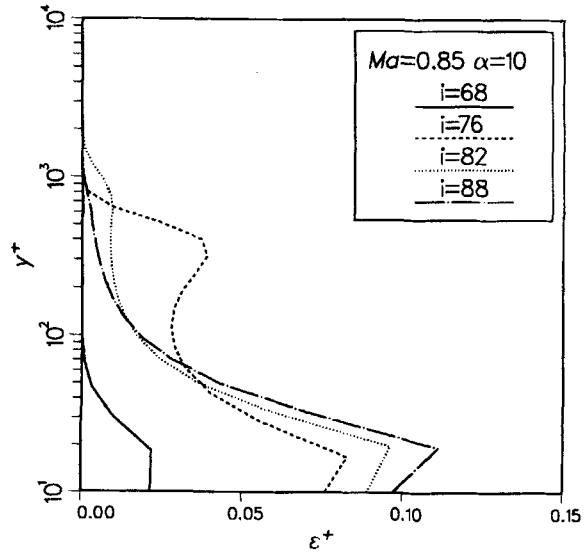

Figure 19. Profiles of dissipation of turbulence at $2y/b = 0{\cdot}27$

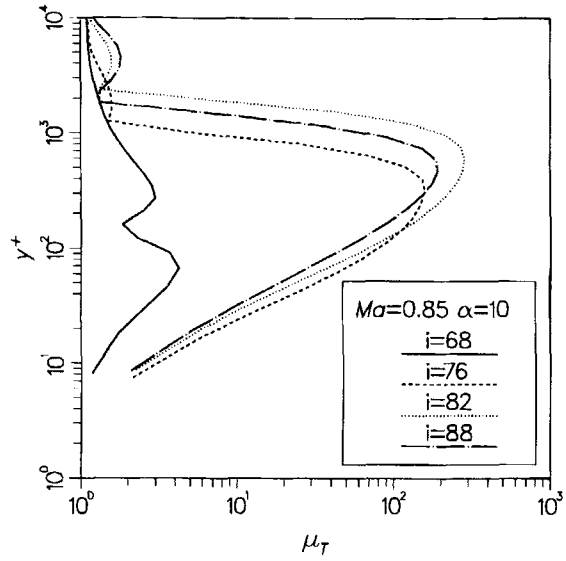

Figure 20. Turbulent viscosity profiles at $2y/b = 0{\cdot}27$

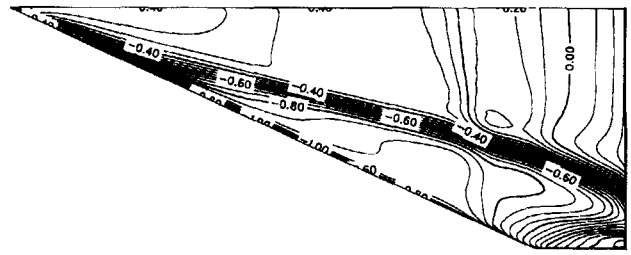

Figure 21. Pressure coefficient distribution on the upper surface of the delta wing

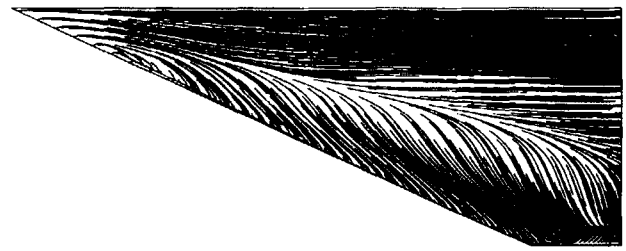

Figure 22. Surface streamlines on the upper surface of the delta wing

similar curves except for the station $i = 68$, where the turbulent viscosity has a low value. By comparing the turbulence kinetic energy profiles and μ_T profiles, it can be seen that on the outer edge of the boundary layer, where k approaches the free-stream value, which is practically zero in this case, turbulent viscosity has a spurious second maximum. This is caused by the fact that the dissipation of turbulence approaches its free-stream value faster than k. The behaviour of μ_T on the edge of the boundary layer is not correct, but its effect on the flow field was assumed to be small, since the velocity gradient is small outside the boundary layer. The clearly unphysical behaviour of μ_T could be corrected

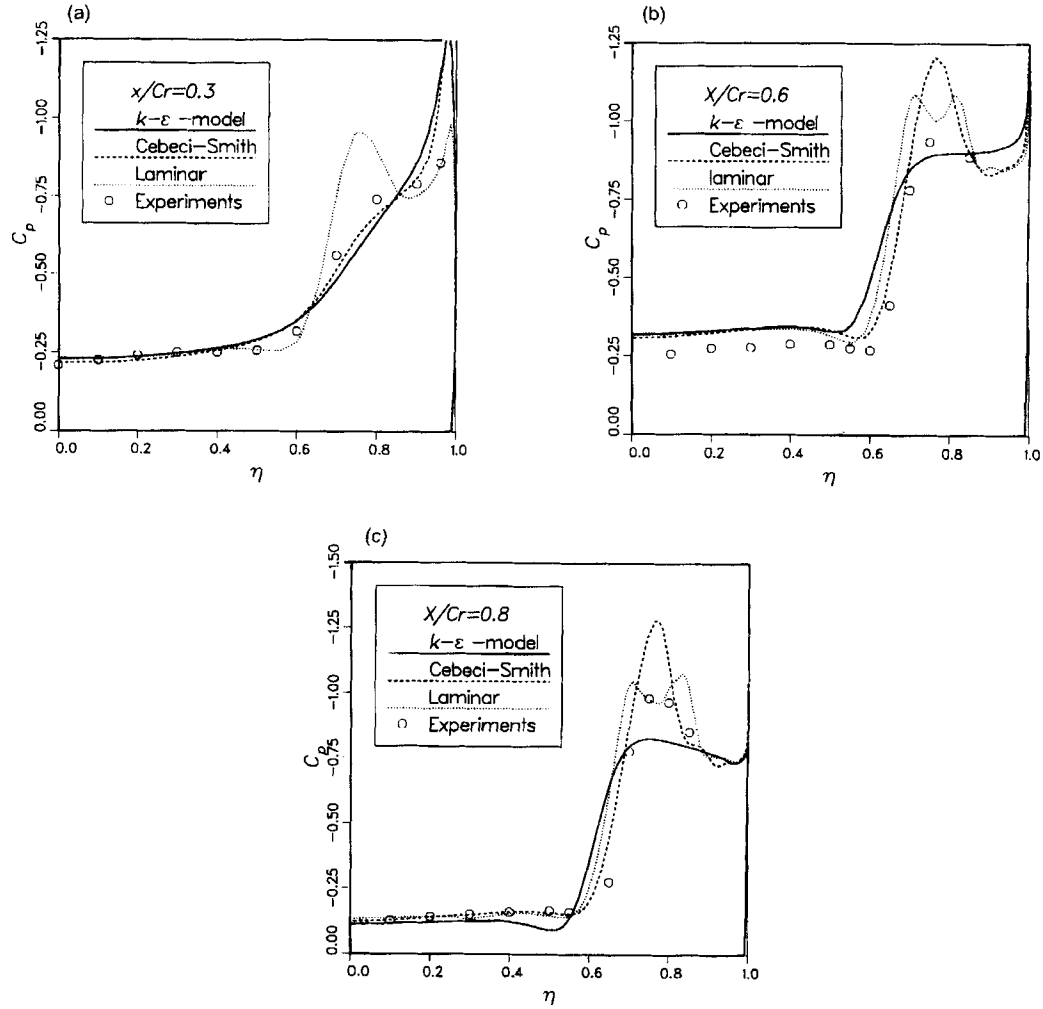

Figure 23. Pressure coefficient distributions at $Re = 4{\cdot}5 \times 10^6$, $\alpha = 10{\cdot}76°$ using k-ε model, laminar flow assumption and the Cebeci–Smith model[17]: (a) $x/c_r = 0{\cdot}3$, (b) $x/c_r = 0{\cdot}6$, and (c) $x/c_r = 0{\cdot}8$. The experimental results are from Reference 15

by adding a suitable constant to the denominator of (15). A better way is to establish an appropriate treatment for the free-stream values of the turbulence quantities.

The pressure coefficient distribution on the upper surface of the wing is shown in Figure 21, and Figure 22 shows surface streamlines on the upper surface. Compared with the results in Reference 17, the vortex is wider than that obtained using the Cebeci–Smith model. Only one vortex is formed, whereas the results in Reference 17 showed also a clear secondary separation line with the associated secondary vortex.

In Figure 23 the calculated and experimental pressure coefficient distributions at cross sections $x/c_r = 0{\cdot}3$, $0{\cdot}6$ and $0{\cdot}8$ are compared. The comparison confirms the conclusion made according to Figures 21 and 22. The suction peak is smeared mainly due to high turbulent viscosities inside the primary vortex. The quality of the k-ε result seems to be poor in comparison with the laminar or Cebeci–Smith prediction. On the other hand, it should be noted that the quantitative difference between the experimental data and the Cebeci–Smith simulation is larger than the corresponding difference

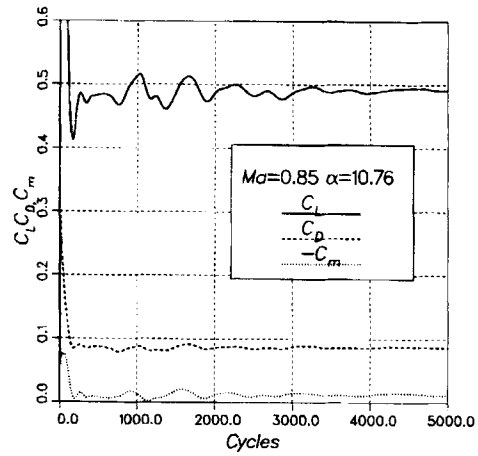

Figure 24. Convergence of the lift, drag and pitching moment coefficients using a single grid

between the data and k-ε results. Probably the results of both simulations could be improved if transition were taken into account.

This case was calculated twice: first using only a single grid, and for a comparison of convergence the second calculation was performed using three grid multigrid levels. The Courant number was 1·0 in both calculations. Using only one grid level, approximately 5 000 iteration cycles were required to obtain a sufficiently converged result, whereas with three multigrid levels a sufficiently converged result was obtained within 1 000 cycles. The convergence history of the aerodynamic coefficients using a single grid is given in Figure 24. The convergence of the coefficients reveals a typical feature for the present flow case: the flow is oscillatory and actually no steady state could be obtained. After about 5 000 cycles the monitored turbulence quantities were almost frozen and the computation was stopped.

4. CONCLUSIONS

The Reynolds-averaged Navier–Stokes equations with a low-Reynolds number k-ε turbulence model have been solved using an implicit method with a multigrid acceleration for convergence. In the evaluation of fluxes the turbulence equations are coupled with the inviscid part of the flow equations in the eigenvector analysis utilized with Roe's method. The effect of this complete coupling was not studied, but is probably small in the present test cases. The implicit stage is based on the approximate factorization, and the source term of the turbulence equations is factored out of the spatial sweeps. A few limitations were added into the original scheme because of the k-ε turbulence model. With these limitations, the stability properties of the scheme with the k–ε model are about the same as in the case of an algebraic turbulence model.

In the multigrid cycle the turbulent viscosities on the coarse grid levels are interpolated from the densest level. This treatment is essential for the robustness of the multigrid method. In addition, similar limitations, as in the case of the implicit stage, are applied for the correction of the turbulence variables inside the multigrid cycle. When the multigrid is used the convergence is significantly enhanced. However, in spite of all the remedies, in some cases the multigrid method cannot be applied or at least the number of grid levels has to be reduced from the maximum possible. It should be noted that sometimes this reduction has to be made in tough cases, even with an algebraic model.

The overall conclusion is that with the k-ε model, convergence is slower than with an algebraic model. This is probably caused by the slow development of the turbulence quantities and the resulting turbulent viscosity. The convergence and the solution are influenced by the initial conditions. Turbulent initial conditions can be used to speed up the convergence. As a result, a fully turbulent solution is obtained. With laminar initial conditions, together with turbulent free-stream conditions, a turbulent solution is also obtained, but the number of iteration cycles is much higher than with suitably chosen initial conditions. If, in addition to the initial conditions, the free-stream conditions correspond to laminar flow, the solution remains laminar, since the model does not contain any device to generate turbulence from a totally laminar flow.

The k-ε model was applied for three test cases. A simple boundary layer is fairly well predicted with the present model. Some improvement was obtained in the case of a 2D transonic airfoil calculation in comparison with an algebraic turbulence model. However, in the case of the delta wing, the results were worse than with algebraic models. The effect of the free-stream values on the turbulence quantities was not evaluated in this study. Proper free-stream conditions may have a large effect on the results and also on the robustness of the algorithm, since many difficulties originate in the region between the turbulent boundary layer and the essentially laminar free-stream. The transition was not taken into account in any of the present test cases. It seems that the treatment of transition is difficult with the k-ε model. This may limit the applicability of the model as well as the applicability of the algebraic Reynolds stress model in aerodynamic simulations.

REFERENCES

1. Launder, B. E. and Spalding, B., *Mathematical models of turbulence*, Academic Press, New York, 1972.
2. Baldwin, B. S. and Lomax, H., Thin layer approximation and algebraic model for separated turbulent flows, *AIAA Paper* 78-257, Jan., 1978.
3. Herng, L. and Ching-Chang, C. Comparison of TVD schemes for turbulent transonic projectile aerodynamics computations with a two-equation model of turbulence, *Int. j. numer. methods fluids*, **16**, 365–390 (1993).
4. Davidson, L. and Rizzi, A., Navier–Stokes stall predictions using an algebraic Reynolds stress model, *J. Spacecraft Rockets*, **29**, 794–800 (1992).
5. Chien, K., Predictions of channel and boundary-layer flows with a low-Reynolds-number turbulence model, *AIAA J.*, **20**, 33–38 (1982).
6. Roe, P. L., Approximate Riemann solvers, parameter vectors, and difference schemes, *J. Comput. Physics*, **43**, 357–372 (1981).
7. Lombard, C. K., Bardina, J. and Venkatapathy, E., Multi-dimensional formulation of CSCM—an upwind flux difference eigenvector split method for the compressible Navier–Stokes equations, In *Proc. 6th AIAA Computational Fluid Dynamics Conference*, Danvers, Massachusetts, 1983.
8. Siikonen, T., Hoffren, J. and Laine, S., A multigrid LU factorization scheme for the thin-layer Navier–Stokes equations, in *Proc. 17th ICAS Congress*, Stockholm, 1990.
9. Vandromme, D., Turbulence modeling for turbulent flows and implementation in Navier–Stokes solvers, in *Introduction to the modeling of turbulence*, VKI Lecture Series 1991–02.
10. Jameson, A. and Yoon, S., Multigrid solution of the Euler equations using implicit schemes, *AIAA J.*, **24**, 1737–1743 (1986).
11. Klebanoff, P. S., Characteristics of turbulence in a boundary layer with zero pressure gradient, *NACA Report 1247*, 1955.
12. Houghton, E. L. and Carruthers, N. B., *Aerodynamics for engineering students*, Edward Arnold, London, 1986.
13. Holst, T. L., Viscous transonic airfoil workshop compendium of results, *J. Aircraft*, **25**, 1073–1087, (1988).
14. Stock, H. W. and Haase, W., Determination of length scales in algebraic turbulence models for Navier–Stokes methods, *AIAA J.*, **270**, 5–14 (1989).
15. *Proceedings of the Symposium on International Vortex Flow Experiment on Euler Code Validation*, Edited by A. Elsenaar and G. Eriksson, Stockholm, Sweden, 1986.
16. Laine, S., Siikonen, T. and Kaurinkoski, P., Calculation of transonic viscous flow around a delta wing, *18th ICAS Congress*, Beijing, 1992.
17. Kaurinkoski, P. and Siikonen, T., Calculation of laminar and turbulent flow past a delta wing, *Helsinki University of Technology, Laboratory of Aerodynamics, Report A-13*, 1992.